Bioactive Materials 13 (2022) 179–190

Contents lists available at ScienceDirect

Bioactive Materials

journal homepage: www.keaipublishing.com/en/journals/bioactive-materials

Self-anti-angiogenesis nanoparticles enhance anti-metastatic-tumor efficacy of chemotherapeutics

Jiamao Luo [a,b], Xinxian Zhong [a,b], Yingming Peng [b], Chenyuan Hao [a,b], Xiaomei Liang [a,b], Yulu Yang [a,b], Xiubo Shi [b], Xuncai Chen [c], Xiao Yi [a], Xiaoxuan Li [a], Jianhua Wu [b], Jinheng Li [b], Qian Xiao [b], Chentian Wu [b], Ruojing Lu [b], Yao Pan [b], Xuejiao Wang [b], Jun-Bing Fan [b,***], Yifeng Wang [a,**], Ying Wang [a,b,*]

[a] Department of Obstetrics & Gynecology, Zhujiang Hospital, Southern Medical University, Guangzhou, 510280, China
[b] Guangzhou Key Laboratory of Tumor Immunology Research, Cancer Research Institute, School of Basic Medical Sciences, Southern Medical University, Guangzhou, 510515, China
[c] Department of Forensic Toxicology, School of Forensic Medicine, Southern Medical University, Guangzhou, 510515, China

ARTICLE INFO

Keywords:
self-anti-angiogenesis
Nanoparticles
Metastatic ovarian cancer
VM
EDV

ABSTRACT

Beyond traditional endothelium-dependent vessel (EDV), vascular mimicry (VM) is another critical tumor angiogenesis that further forms in many malignant metastatic tumors. However, the existing anti-angiogenesis combined chemotherapeutics strategies are only efficient for the treatment of EDV-based subcutaneous tumors, but remain a great challenge for the treatment of in situ malignant metastatic tumor associated with EDV and VM. Here, we demonstrate a self-assembled nanoparticle (VE-DDP-Pro) featuring self-anti-EDV and -VM capacity enables to significantly enhance the treatment efficacy of cisplatin (DDP) against the growth and metastasis of ovarian cancer. The VE-DDP-Pro is constructed by patching DDP loaded cRGD-folate-heparin nanoparticles (VE) onto the surface of protamine (Pro) nanoparticle. We demonstrated the self-anti-angiogenesis capacity of VE-DDP-Pro was attributed to VE, which could significantly inhibit the formation of EDV and VM by regulating signaling pathway of MMP-2/VEGF, AKT/mTOR/MMP-2/Laminin and AKT/mTOR/EMT, facilitating chemotherapeutics to effectively suppress the development and metastasis of ovarian cancer. Thus, combing with the chemotherapeutics effectiveness of DDP, the VE-DDP-Pro can significantly enhance treatment efficacy and prolong median survival of mice with metastatic ovarian cancer. We believe our self-assembled nanoparticles integrating the *anti*-EDV and *anti*-VM capacity provide a new preclinical sight to enhance the efficacy of chemotherapeutics for the treatment malignant metastasis tumor.

1. Introduction

Anti-tumor metastasis remains a major challenge to the tumor treatment because of rapid growth and proliferation of active tumor cells. The newly formed tumor angiogenesis provides a more efficient avenue for the tumor metastasis [1,2]. Tumor angiogenesis usually involves endothelium-dependent vessels (EDV) which almost formed in solid tumors, enabling to provide oxygen and nutrition for tumor growth, development and metastasis. Accompanying with the further proliferation of tumor, especially in many malignant metastatic tumors, another critical tumor angiogenesis of vascular mimicry (VM) would be formed *via* the proliferation of highly aggressive tumor cells [3–5]. Recent advances have suggested VM could significantly promote distant metastasis and the migration of tumor cells, which is directly responsible for the most of cancer deaths [6]. Consequently, VM has been identified as an independent adverse prognostic factor for 5-year survival, tumor staging and metastasis in clinical tumor treatment [7,8]. Traditional anti-tumor therapy has mainly concerned on the combination chemotherapeutic drug with *anti*-EDV drug (such as bevacizumab) to suppress tumor cell proliferation [9–14]. However, these strategies often meet great challenge in the treatment of those malignant metastatic tumors

Peer review under responsibility of KeAi Communications Co., Ltd.
* Corresponding author. Department of Obstetrics & Gynecology, Zhujiang Hospital, Southern Medical University, Guangzhou, 510280, China.
** Corresponding author.
*** Corresponding author.
E-mail addresses: fjb2012@mail.ipc.ac.cn (J.-B. Fan), wangyifeng@smu.edu.cn (Y. Wang), ningmengquan@gmail.com (Y. Wang).

https://doi.org/10.1016/j.bioactmat.2021.10.037
Received 3 June 2021; Received in revised form 8 September 2021; Accepted 26 October 2021
Available online 2 November 2021

Abbreviations

AKT	Protein Kinase B
CH_{50}	complement hemolysis 50%
cRGD	cyclic RGD peptide
Cy3	cyanine3
Cy7	cyanine7
DDP	cisplatin
DLS	dynamic lighting scatter
E-cad	E-cadherin
EE	encapsulation efficiency
EDV	endothelium-dependent vessel
ELISA	enzyme linked immunosorbent assay
EMT	Epithelial-Mesenchymal Transition
FBS	Feta Bovine Serum
FTIR	fourier transform infrared spectra
FR	folate receptor
H&E	hematoxylin-eosin
^{1}H NMR	^{1}H nuclear magnetic resonance
HUVEC	human umbilical vein endothelial cells
IC_{50}	half maximal inhibitory concentration
LE	loading efficiency
Luc	Luciferase
ICP-MS	inductively coupled plasma mass spectrometry
MMP-2	Matrix Metalloproteinase-2
MPS	mononuclear phagocyte system
mTOR	Mammalian Target of Rapamycin
MTT	3-(4,5-Dimethylthiazol-2-yl)-2,5-diphenyltetrazolium bromide
p-AKT	Phospho-AKT
PAS	Periodic Acid-Schiff stain
PBS	phosphate buffered saline
PDI	Poly-dispersity Index
p-mTOR	Phospho-mTOR
Pro	protamine
Pt	platinum
SD	Standard Deviation
SPF	Specific Pathogen Free
TEM	transmission electron microscopy
UV	ultraviolet
VE	cRGD-folate-heparin nanoparticles
VE-DDP-Pro	self-assembled nanoparticle
VEGF	Vascular Endothelial Growth Factor
VEGFA	Vascular Endothelial Growth Factor A
VM	vascular mimicry

associated with EDV and VM [15–18]. Ovarian cancer is prone to metastasis *via* VM formed by rapidly proliferating ovarian cells and tumor vascularization based on EDV throughout the peritoneal cavity. Although cisplatin (DDP) is one of the most effective chemotherapeutic drugs for ovarian cancer, the current strategy on combining DDP-based chemotherapy with EDV-based anti-angiogenesis does not seem to improve patient survival. Moreover, most of experimental efforts have attempted to focus on subcutaneous tumor models (such as subcutaneous ovarian cancer model) rather than clinically relevant tumor models, leading to the inaccurately reflecting primary tumor progression and inefficient treatment strategies, particularly in the case of highly metastatic tumor [19]. Thus, it is a critical need for new combination strategies to inhibit tumor cell proliferation and angiogenesis for the highly treatment of in situ malignant tumor enabling to spontaneously produce metastatic tumors associated with EDV and VM.

It was reported cRGD binding with integrin $\alpha_v\beta_3$ or $\alpha_5\beta_1$ could present promising *anti*-EDV capability by down-regulating MMP-2/VEGF expression [20]. Meanwhile, cRGD binding with integrin $\alpha_v\beta_3$ could not only decrease the phosphorylation of AKT/mTOR/MMP-2 and increase the expression of Laminin5γ2, but also could reduce epithelial-mesenchymal transition (EMT) thereby inhibiting VM formation in ovarian cancer cells [21]. We previously used heparin conjugated with folate and cRGD to fabricate cRGD-folate-heparin nanoparticle (VE nanoparticle) [22]. In particular, it was found that when the dose of cRGD peptide was above 15% (w:w) within VE nanoparticles, the nanoparticles can achieve the *anti*-EDV and *anti*-VM ability in ovarian cancer. Herein, we demonstrate a self-assembled nanoparticle (VE-DDP-Pro) that integrates DDP triggered anti-proliferation and VE nanoparticle induced self-*anti*-EDV and -VM, enabling to effectively suppress the growth and metastasis of malignant ovarian cancer. In designing our system, the fabrication of VE-DDP-Pro was prepared by a two-steps self-assembly strategy. VE nanoparticle with *anti*-VM and *anti*-EDV capacities was firstly fabricated by a self-assembly of heparin, cRGD and folate. It was reported that folate receptor (FR) is overexpressed in many human cancer cells, including malignancies of the ovary, brain, kidney, breast, myeloid cells, and lung [23,24]. Thus dual targeting ligands, cRGD peptide and folate, can specifically bind with overexpressed integrins $\alpha_v\beta_3$ and $\alpha_5\beta_1$ and FR in tumor cell to enhance the targeting [23–27]. DDP was subsequently chelated onto VE nanoparticle to fabricate VE-DDP nanoparticle resulting in enhancing the anti-proliferation capacity. Furthermore, protamine (Pro) was used to collect VE-DDP nanoparticle to generate VE-DDP-Pro nanoparticle for increasing its transmembrane capacity by an electrostatic interaction. Under the acidic microenvironment of the tumor, positive-charged protamine within nanoparticle easily absorbed with H^+ [28,29] and dissociated from VE-DDP-Pro, leading to release of VE-DDP into ovarian cancer cells. The released VE-DDP could differentially bind integrins $\alpha_v\beta_3$ or $\alpha_5\beta_1$ to regulate AKT/mTOR/MMP-2/Laminin and AKT/mTOR/EMT signaling pathway, triggering *anti*-VM. Meanwhile, downregulation of MMP-2 would also inhibit the release of VEGF, enabling the obtained VE-DDP to trigger *anti*-EDV. Simultaneously, DDP could induce DNA damage, resulting in the apoptosis of ovarian cancer cells (Scheme 1).

In anti-tumor experiments of in situ ovarian cancer mouse model, both control group and DDP group further developed the distant metastasis though DDP group could suppress the growth of ovarian cancer at the early stage, which was in accordance with clinical ovarian cancer progression and the current treatment status of DDP. While, our VE-DDP-Pro exhibit superior self-anti-EDV and -VM capacities by regulating signaling pathways of AKT/mTOR/MMP-2/Laminin, AKT/mTOR/EMT, and MMP-2/VEGF expression, and thereby greatly enhancing the anti-ovarian cancer efficacy by combing with DDP chemotherapeutics. Thus our self-assembled VE-DDP-Pro could specifically deliver DDP to ovarian cancer, significantly increase drug accumulation in tumor, and efficiently improve their bioavailability *in vivo*, thereby presenting the sustaining capacity to suppress the deterioration and metastasis of ovarian cancer.

2. Materials and methods

2.1. Preparation of nanoparticles

VE was prepared according to a previously documented method [22]. cRGD and folate concentrations of VE were separately determined using the CQBCA protein quantitation Kit and UV spectrometer (Shimadzu, UV-2600). VE solution (1 mL, n = 3) was lyophilized to exclude excess water, generating a light yellow powder (2.57 ± 0.12 mg). The heparin concentration of VE was calculated based on the following

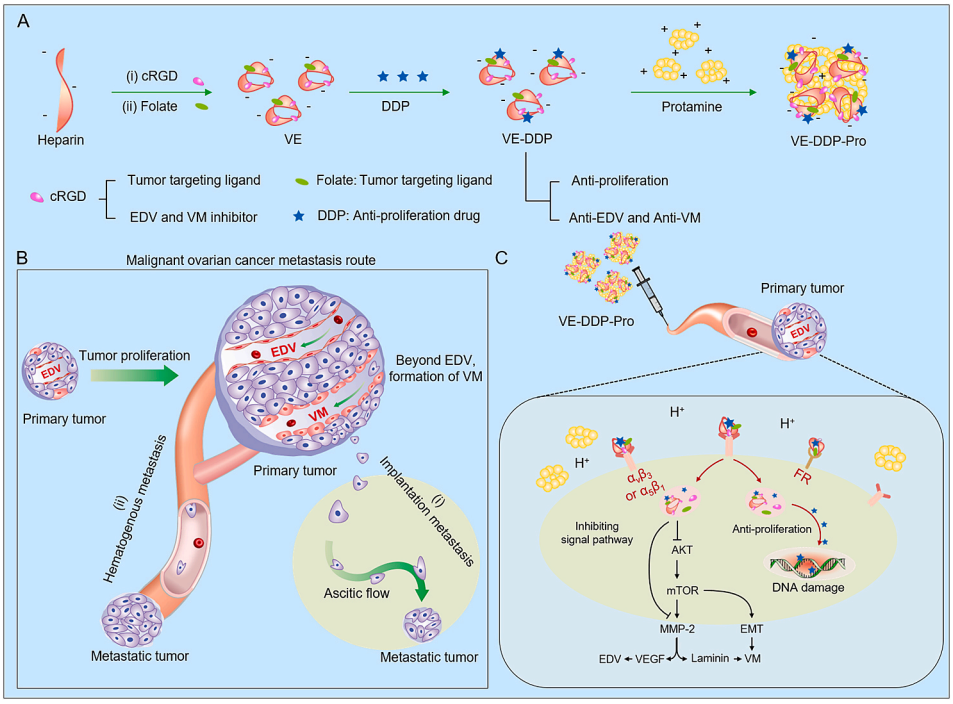

Scheme 1. Rational design of self-assembled nanoparticle (VE-DDP-Pro) with anti-proliferation, *anti*-EDV and *anti*-VM capacities for the efficient treatment against ovarian cancer. (A) Fabrication of VE-DDP-Pro. VE was firstly prepared *via* self-assembly strategy by employing heparin conjugated with cRGD and folate. DDP subsequently was chelated to VE to prepare VE-DDP nanoparticle. And then protamine was used to collect VE-DDP nanoparticle to fabricate VE-DDP-Pro nanoparticle for the increase of the transmembrane capacity. (B) Malignant ovarian cancer metastasis route associated with EDV and VM. Implantation-metastasis and hematogenous metastases are key events in growth and metastasis of ovarian cancer. (C) The therapeutic mechanism underlying VE-DDP-Pro-mediated inhibition of ovarian cancer metastasis. Positively charged Pro dissociates from VE-DDP-Pro to release VE-DDP under a tumor acidic microenvironment, which differentially binds integrin $\alpha_v\beta_3$ or $\alpha_5\beta_1$ to regulate the AKT/mTOR/MMP-2/Laminin, AKT/mTOR/EMT signaling pathways, and downregulation of MMP-2 additionally inhibits release of VEGF, thereby synergistically exerting *anti*-VM and *anti*-EDV effects. Simultaneously, DDP induces DNA damage resulting in cancer cell apoptosis.

equation: concentration of heparin = (weight of VE-weight of cRGD and weight of folate)/1 mL. LE of heparin, folate and cRGD was calculated as follows: LE = (weight of loaded drug in nanoparticles)/(weight of nanoparticles) × 100%. For preparation of VE-DDP, DDP (0.90 mg, 5% DDP/heparin weight ratio) was added into VE (10 mL, [heparin] = 1.80 mg/mL) solution under gentle stirring at room temperature for 24 h in the dark. Free DDP was removed *via* dialysis against distilled water for 48 h. VE-DDP-Pro was prepared by simple mixing of VE-DDP and protamine solution. Protamine was prepared in deionized water at a concentration of 5 mg/mL. Protamine (1.08 mL; 30% Pro/Heparin weight ratio) solution was added into VE-DDP solution (10 mL, [heparin] = 1.80 mg/mL) prepared beforehand and VE-DDP-Pro solution subjected to ultrasonication for 30 min. DDP concentrations of VE-DDP and VE-DDP-Pro solutions were measured *via* ICP-MS. The following formulae were used to calculate encapsulation efficiency (EE) and loading efficiency (LE) of DDP: EE = (weight of loaded drug)/(weight of initially added drug) × 100%; LE = (weight of loaded drug in nanoparticles)/(weight of nanoparticles) × 100%. VE, VE-DDP and VE-DDP-Pro in 10% FBS solution were prepared by separately adding 1 mL FBS into 9 mL VE, VE-DDP and VE-DDP-Pro water solutions. Different DDP/heparin (VE-DDP) and Pro/Heparin weight ratios (VE-DDP-Pro) were obtained using the procedure specified above. Cy3-NH_2 or Cy7-NH_2 labeled VE, VE-DDP and VE-DDP-Pro were additionally prepared in a similar manner. We used visible-light dye Cy3 to detect the bio-function of drug delivery system *in vitro*. To avoid the interference of auto-fluorescence in living body, the near-infrared dye Cy7 was used to label drug delivery system and investigate their *in vivo* bio-function.

2.2. Anti-C3a activation in vitro

To assess complement activation *in vitro*, we measured complement activation fragment C3a, the common product of three complement activation pathways, by ELISA. Human serum was donated by healthy voluntaries. Written informed consent was obtained from all participants. The experiment was carried out in accordance with the approved guidelines. In a typical experiment we mixed VE (2 mg), VE -DDP, VE -DDP-Pro (containing 2 mg VE), respectively, with 2 mL undiluted serum in tubes, which were then incubated for 1 h at 37 °C in a shaking water bath (80 rpm). After incubation, the mixture was centrifuged at 3000 rpm for 10 min. The supernatant was used to detect the C3a concentration using commercially available human C3a ELISA kits according to the manufacturer's instruction. The experiment was performed in triplicate and the result displayed a representative of three independent experiments.

2.3. Complement hemolysis activity in vitro

The hemolytic activity of the biomaterials was investigated according to a modified CH_{50} method of Mayer. It measured total hemolytic activity of the classical and terminal pathways using sensitized sheep erythrocytes. Human serum was donated by healthy voluntaries. Written informed consent was obtained from all participants. The serum was diluted with barbital buffer solution pH = 7.4 in the ratio of 1:20. Sensitized sheep erythrocytes was made of 2% sheep erythrocyte suspension (20 mL) which was incubated for 30 min with an equal volume of hemolysin (rabbit anti-sheep red blood cell antibody) at 37 °C. In a typical experiment, we mixed VE (200 μg), VE-DDP, VE-DDP-Pro (containing 200 μg VE), respectively, with 3 mL 1:20 diluted serum in tubes, which were then incubated for 1 h at 37 °C in a shaking water bath (80 rpm). And then, the sensitized sheep erythrocytes (1 mL) was incubated for 30 min with different mixture serums in serial volumes according to the manufacturer's instruction at 37 °C. After incubation, samples were centrifuged at 2000 rpm for 10 min to obtain supernatant, containing free hemoglobin. The hemoglobin concentration was measured by a spectrophotometer at 542 nm. Positive reference was 50% lysis diluted by total lysis, and negative reference was obtained after incubation with buffer. The complement content of each sample could be calculated by the following formula: complement content CH_{50} (U/mL) = (1/sample serum volume) × dilution factor. The experiment was performed in triplicate and the result displayed a representative of three independent experiments.

2.4. Tube formation assay

Tube formation was observed *via* 3D culture. Briefly, 24-well culture

plates were coated with Matrigel Basement Membrane Matrix (0.3 mL per well; BD Biosciences, Franklin Lakes, NJ, USA), and allowed to polymerize for 60 min at 37 °C. Cells were seeded onto the surface of Matrigel (1 mL per well) at a density of 1.5×10^5 cells/mL. To investigate the *anti*-EDV and *anti*-VM abilities of VE, VE-DDP and VE-DDP-Pro, SKOV3 and HUVEC cells were incubated on 3D matrigel, followed by treatment with PBS, VE, VE-DDP or VE-DDP-Pro for 4 days at equivalent concentrations to cRGD (20 μg/mL). Cells treated with PBS were used as the control group. Tubular structures were examined *via* microscopy. Formation of tubes was quantified based on total length (complete structures) and number of intersections (complete structures) per field in five randomly selected fields using image analysis software (Image-Pro Plus, Washington, DC, USA).

2.5. Establishment and identification of the nude mice orthotopic ovarian carcinoma and metastasis model

All animal studies were conducted in accordance with local guidelines on the ethical use of animals and the National Institutes of Health Guide for the Care and Use of Laboratory Animals. Healthy BALB/c female nude mice (15–16 g) were anesthetized *via* intraperitoneal injection with 1% sodium pentobarbital (8 μL/g). An incision of the abdominal cavity was made from the back to expose the right ovary with the left ovary used as a self-control. SKOV3-Luc cells were suspended in ice-cold PBS at a density of 4×10^4 cells/μL and 10 μL slowly injected into ovary tissue using a microsyringe (10 μL). Mice continued to be fed in an SPF environment after surgery and tumor growth was monitored using an *in vivo* imaging system (IVIS Lumina II, Caliper, USA) every 4 days. On day 16 (taking the day of surgery day as 'day 0'), mice were sacrificed, and the whole ovary with primary tumor, metastatic nodules in the peritoneal cavity, metastatic nodules on mesentery, and main organs (heart, liver, spleen, lung, kidney) were isolated to analyze bioluminescence signals. For tracing of ovarian primary tumor development, some mice were sacrificed every 4 days to obtain the whole ovary with primary tumor. Pathological analysis was applied to identify orthotopic ovarian carcinoma in nude mice, indicating successful generation of the metastasis model.

2.6. In vivo biodistribution and tumor targeting ability of nanoparticles

Mice models were constructed as above, and 4 days after surgery, mice were treated with a single dose of free Cy7, Cy7-VE-DDP or Cy7-CE-DDP-Pro (DDP 2 μg/g, three mice per group) *via* tail vein injection. Fluorescence signals were examined at different checkpoints. After 24, 48, 72, 96 and 120 h, mice were sacrificed and their organs and tumors isolated for directly monitoring fluorescence. Tumors of mice obtained at different time-points were used to detect changes in the tumor-targeting ability of nanoparticles over time.

2.7. In vivo ability of nanoparticles to inhibit ovarian cancer proliferation and metastasis

Twenty mice models were generated as specified above and randomly divided into four groups (control, DDP, VE-DDP, VE-DDP-Pro; five mice per group). Mice of the control group were treated with PBS and those of other three groups with DDP, VE-DDP and VE-DDP-Pro (DDP 2 μg/g) *via* tail vein injection. Three days after administration of SKOV3-Luc cells, mice were administered the first treatment and bioluminescence assessed (taken as day 0). Treatments were administered every 3 days and bioluminescence measured every 4 days. Additionally, body weights of mice were recorded every day. On day 20, abdominal circumferences of mice were examined. Mice were sacrificed and ovarian primary tumors, metastatic nodules in the peritoneal cavity, metastatic nodules on mesentery, and main organs (heart, liver, spleen, lung, kidney) were obtained. Bioluminescence signals of ovarian cancer cells were analyzed and proliferation rate calculated as follows: proliferation rate = luminescence signal intensity of day n/average luminescence signal intensity on day 0. After sacrifice of mice, weights and volumes of ovarian primary tumors, metastasis in the peritoneal cavity, ascites formation, bioluminescence and numbers of metastatic nodules on mesentery were analyzed. Tumor volume was calculated as: V = larger diameter × (smaller diameter)^2/2. H&E staining of intestines was applied to confirm metastasis of ovarian cancer cells on mesentery and main organs for evaluation of nanoparticle tolerability.

2.8. Survival analysis

In total, 24 nude mice (administered SKOV3 cells for 3 days) were randomly divided into four groups (control, DDP, VE-DDP and VE-DDP-Pro). Mice of the control group were treated with PBS and those from three other groups with DDP, VE-DDP and VE-DDP-Pro (DDP 2 μg/g, six mice per group) *via* tail vein injection. Treatments were performed every three days until six injections were administered. Kaplan-Meier analysis was applied for plotting the survival curve and the median survival times of each group calculated.

2.9. Immunohistochemical analysis

Ovarian primary tumors and metastatic nodules were embedded in paraffin wax, cut into 3 μm thick sections, and subjected to immunohistochemical analysis of Ki-67, cleaved caspase-3, CD34, MMP-2 and VEGF-A expression or CD34/PAS histochemical double-staining according to standard clinical laboratory protocols. Images of tissues were acquired under an optical microscope (Nikon Eclipse 80i, JAPAN). Ki-67, cleaved caspase-3 and MMP-2 indices were calculated based on the equation: (positive cells in an image/all cells in an image) × 100%. Relative expression of $CD34^+$ structures and VM ($CD34^-/PAS^+$ vascular-like structures) was calculated as follows: relative expression of $CD34^+$ = (number of $CD34^+$ structures of each group/number of $CD34^+$ structures of control group) × 100%; relative expression of VM = (number of $CD34^-/PAS^+$ structures of each group/number of $CD34^-/PAS^+$ structures of control group) × 100%. At least five images were used to calculate the above indices or relative expression levels.

2.10. Statistical analysis

All results are presented as means ± SD. Data were analyzed using Student's t-test or one-way analysis of variance, except where otherwise specified. Differences between groups were considered significant at two-sided P values < 0.05. Statistical analysis was performed using SPSS version 20.0 software.

3. Results and discussion

3.1. Fabrication and characterization of VE-DDP-Pro

VE-DDP-Pro was prepared by a two-steps self-assembly strategy. In brief, VE nanoparticle was chelated with DDP to generate VE-DDP by substituting chlorides of DDP with the carboxyl group of heparin (Fig. S1) [30], and then positively charged protamine (Pro) was used to absorb and compress VE-DDP, thereby fabricating VE-DDP-Pro *via* electrostatic interactions. It was reported that when the chlorides in DDP are substituted with carboxylates, the newly formed carboxylic ligands are still reversible due to their fairly low nucleophilicity [31]. Because carboxylate as a good leaving group can be utilized for designing a tumor-directed carrier system of a cytotoxic platinum complex with carboxylate-containing carriers to achieve selective delivery to tumor sites with prolonged periods of cytotoxic action due to sustained release from carrier through ligand exchange reaction. Thus compared with DDP, the bioactivity of DDP in VE-DDP and VE-DDP-Pro could be enhanced instead after the chelation between DDP and VE.

The introduction of DDP to VE was carried out by varying the

amount of DDP in distilled water. VE structure was characterized by ^{1}H NMR (Fig. S2). As shown in Fig. S3, it was found that 5% DDP/heparin weight ratio of VE-DDP presented better size and polydispersity index (PDI) than other ratios determined by dynamic lighting scatter (DLS). Under this proportion, VE (24.8 ± 3.2 nm) and DDP could assemble into large-sized nanoparticles (VE-DDP, 77.2 ± 1 nm) in distill water. Meanwhile, the fourier transform infrared spectra (FTIR) spectra showed a band at 3294 cm^{-1} decreased in VE-DDP compared in VE, which was assigned to hydroxyl group vibration of carboxyl in heparin (Fig. S4A). The result indicated the chlorides of DDP were substituted with carboxyl of VE to form VE-DDP. We subsequently examined the optimal weight ratio of Pro versus heparin of VE-DDP. It was found that 30% Pro/heparin weight ratio in VE-DDP-Pro exhibited optimized property determined by DLS. Zeta potential showed that VE and VE-DDP had similar potential (−32∼-35 mV), while VE-DDP-Pro had negative potential (−30 mV), suggesting that the negative-charged VE-DDP was exposed on the surface of VE-DDP-Pro due to protamine with positive charge (Fig. S3). FTIR spectra showed compared with VE-DDP the hydroxyl group bands of carboxyl at 3294 cm^{-1} and the sulfate bands of heparin at 1030 and 1230 cm^{-1} were decreased in VE-DDP-Pro [32], indicating positive-charged protamine was successfully absorbed with negative-charged heparin of VE-DDP (Fig. S4B). The DDP encapsulating efficiency of VE-DDP-Pro was about 65% determined by ICP-MS (Fig. S5). The loading efficiency of cRGD, folate and DDP was shown in Table S1. Thus, a 5% weight ratio of DDP/heparin in VE-DDP and a 30% weight ratio of Pro/heparin in VE-DDP-Pro were served as the optimized formulation and employed for subsequent experiments.

We subsequently investigated the stability of the optimized formulations in mimic blood conditions (10% FBS) using DLS and transmission electron microscopy (TEM). It showed VE (26.9 ± 1.2 nm) and VE-DDP (47.4 ± 1 nm) were uniform spherical nanoparticles in 10% FBS (Fig. 1A–B). Interestingly, protamine exhibited spherical shape with small size in 10% FBS (Fig. 1C). When VE-DDP was collected by protamine, the size of the obtained VE-DDP-Pro was increased to 187 ± 3.5 nm in 10% FBS and the morphology of VE-DDP-Pro presented monodispersed larger sphere (Fig. 1D–E, S3B). It showed VE-DDP adhered to the outer layer and Pro located in the inner layer in Fig. 1D. In our study, we found VE, VE-DDP and VE-DDP-Pro exhibited excellent stability in 10% FBS at pH 7.4, through which their size was nearly unchanged within a 72 h period (Fig. S6). It was reported that the pH value of tumor microenvironment is approximately 6.5, which is lower than the pH of 7.4 in normal tissues, while late endosomes and lysosomes have much lower pH, in the range 4.5–5.5 [29,33,34]. The decomposition of drug delivery systems at a decreased pH could accelerate the drug release at tumor sites and thus enhance the therapeutic effect to tumor cells and minimize the toxic side effects to normal cells [29,34]. Thus, we employed pH of 7.4 and 5.5 to investigate the stability of VE-DDP-Pro. As shown in Fig. 1H, I and J, compared with VE-DDP-Pro in 10% FBS at pH 7.4 (size, 190 ± 10 nm, PDI, 0.1), VE-DDP-Pro in 10% FBS at pH 5.5 exhibited changed morphology with the decreased sizes (116 nm ± 40 nm, PDI, 0.4). Because protamine is a positive-charged protein, it can easily bind with H^+ under acidic condition to reduce the interaction with VE-DDP, leading to the dissociation of VE-DDP-Pro. This result indicated that the acidic environment was beneficial to the release of VE-DDP from VE-DDP-Pro *via* electrostatic dissociation [28,29,35,36]. Based on anti-complement activation of heparin, we further investigated the complement activation capacity of VE, VE-DDP and VE-DDP-Pro by measuring C3a concentration (a key complement activation component) and the complement hemolysis 50% (CH_{50}) in blood serum (Fig. 1F and G). The results showed these nanoparticles possessed significant effects on anti-complement system activation, which would be beneficial to reduce opsonization by MPS and improve bioavailability.

3.2. Cellular uptake ability of VE-DDP-Pro

We next investigated the biological functions of VE-DDP-Pro *in vitro*, including targeting ability, cytotoxicities, *anti*-EDV and *anti*-VM capacities. It was reported that cRGD could specifically bind with integrins of $\alpha_v\beta_3$ and $\alpha_5\beta_1$, which are overexpressed on neovascular endothelial cells

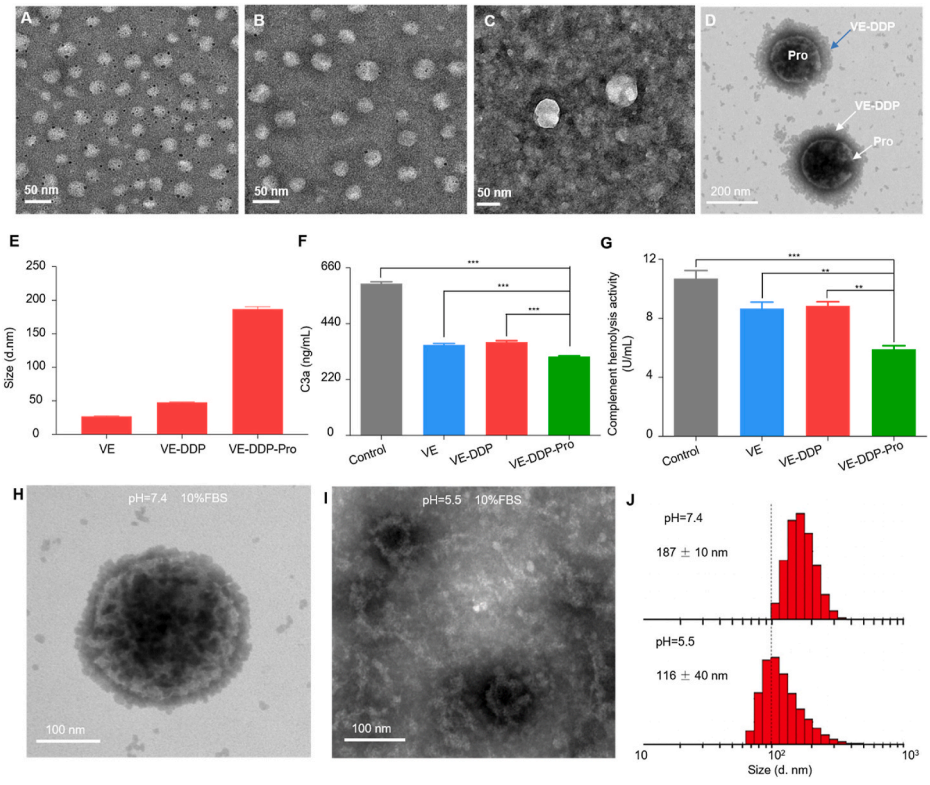

Fig. 1. Fabrication and characterization of VE-DDP-Pro. (A to D) TEM images of the VE, VE-DDP, protamine and VE-DDP-Pro in 10% FBS. (E) DLS characterization of the sizes of VE, VE-DDP and VE-DDP-Pro in 10% FBS. (F to G) Anti-complement system activation ability of VE, VE-DDP and VE-DDP-Pro. The contents of C3a in the blood serum samples were examined *via* ELISA and complement hemolysis activity were tested by CH_{50} assay. Data are presented as means ± SD (n = 3), $^{**}P < 0.01$, $^{***}P < 0.001$. (H to I) TEM images of VE-DDP-Pro in 10% FBS solution at pH 7.4 and pH 5.5, respectively. (J) The sizes of VE-DDP-Pro in 10% FBS at pH 7.4 and pH 5.5, respectively. Compared with VE-DDP-Pro in 10% FBS at pH 7.4 (size, 187 nm ± 10 nm, PDI, 0.1), VE-DDP-Pro in 10% FBS at pH 5.5 showed looser architectures and the sizes decreased to 116 nm ± 40 nm with a higher PDI (PDI, 0.4).

of some tumors and low expression on normal tissues, and FR is over-expressed in ovarian cancer cells [23,24,37,38]. Here, we firstly evaluated $\alpha_v\beta_3$, $\alpha_5\beta_1$ and FR-α expression in two human ovarian cancer cells (SKOV3 and A2780), human umbilical vein endothelial cells (HUVEC), and normal human ovary cells (IOSE-80) *via* Western blot (Fig. S7). It detected high expression of $\alpha_v\beta_3$, $\alpha_5\beta_1$ and FR-α in SKOV3 cells and α_v, β_1 and FR-α in A2780 and HUVEC cells while α_v expression was partly detected in IOSE-80 cells. Thus, we chose IOSE-80 cells as a negative control in subsequent cellular uptake and cytotoxicity experiments. And then fluorescent dye Cy3-NH_2 was conjugated with carboxyl group of heparin in folate-heparin, cRGD-heparin, cRGD-folate-heparin (VE), VE-DDP and VE-DDP-Pro to detect their cellular uptake ability by flow cytometry. The results showed cRGD-folate-heparin exhibited the best cellular uptake ability in these cell lines (Fig. S8A). The cellular uptake of Cy3-VE, Cy3-VE-DDP and Cy3-VE-DDP-Pro was investigated by flow cytometry and laser scanning confocal imaging, respectively. As show in Fig. S8B, their cellular uptake abilities of the four cell lines were in the order: SKOV3 > A2780 > HUVEC > IOSE-80, which was attributable to the expression of $\alpha_v\beta_3$, $\alpha_5\beta_1$ and FR-α. The cellular uptake of VE-DDP-Pro was markedly higher than that of VE-DDP and VE because of the cytomembrane penetration effect of protamine. Laser scanning confocal imaging disclosed that VE and VE-DDP were observed in the cytoplasm for these cells, while VE-DDP-Pro was distributed in cytoplasm and nucleus in SKOV3, A2780 and HUVEC cells (Fig. 2A).

3.3. Cytotoxicity of VE-DDP-Pro

The cytotoxicity of VE, DDP, Pro, VE-DDP and VE-DDP-Pro were subsequently examined *via* 3-(4,5-Dimethylthiazol-2-yl)-2,5-diphenyltetrazolium bromide (MTT) assay (Fig. 2B). The half maximal inhibitory concentration (IC_{50}) values were calculated and standardized by DDP concentration (Table S2). The results showed that the cytotoxicity of VE-DDP-Pro and VE-DDP were obviously higher than that of DDP for SKOV3, A2780 and HUVEC cells, while no significant differences were observed among DDP and VE-DDP for IOSE-80 cells. The levels of cytotoxicity of VE-DDP and VE-DDP-Pro against the four cell lines were established as: SKOV3 (IC_{50}: 3.43 ± 0.61 μg/mL) > HUVEC (IC_{50}: 6.50 ± 0.87 μg/mL)> A2780 (IC_{50}: 9.42 ± 1.09 μg/mL) > IOSE-80(IC_{50}: 14.60 ± 1.09 μg/mL), indicating VE-DDP-Pro presented greater cytotoxicity to cancer cells compared to normal cells. Also, VE, Pro and VE-Pro with equivalent concentration had no obvious cytotoxicity in four cell lines (Fig. S8C). Simultaneously, ICP-MS detected Pt concentration of DDP, VE-DDP and VE-DDP-Pro was 12.51 ± 0.67 ng/10^6 cells, 20.54 ± 0.64 ng/10^6 cells and 35.49 ± 0.56 ng/10^6 cells in SKOV3 cells (Fig. S9), indicating the introduction of protamine could further increase DDP concentration of VE-DDP-Pro thereby presenting superior cytotoxicity in SKOV3 cells. Therefore, we chose SKOV3 cells for the subsequent experiments owing to their remarkable bio-function by VE-DDP-Pro.

3.4. Anti-EDV and -VM ability of VE-DDP-Pro in vitro

Next, the microtube formation experiment by using HUVEC cells was performed to investigate the *anti*-EDV activities of VE, VE-DDP and VE-DDP-Pro while the experiment by using SKOV3 cells was performed to verify their *anti*-VM activities. HUVEC and SKOV3 cells were respectively incubated on 3D matrigel and treated with PBS, DDP, VE, VE-DDP and VE-DDP-Pro with the same concentration of DDP. The cell viability in HUVEC and SKOV3 was above 80% under the selected concentration of DDP, VE-DDP and VE-DDP-Pro. The formation of tubular structures was observed by optical microscopy. As shown in Fig. 2C–D, a large number of tubular structures could be obviously observed in the control group and DDP group, while only a few of tubular structures were observed in the VE, VE-DDP and VE-DDP-Pro. Compared to the control group (100% ± 6.7 for HUVEC cells and 99.4% ± 5.6 for SKOV3 cells) and DDP group (64.1% ± 8 for HUVEC cells and 55.6% ± 2.6 for SKOV3 cells), the tube formation rate was much low in VE (32.6% ± 6.5 for HUVEC cells and 40.9% ± 3.3 for SKOV3 cells) and VE-DDP (15.4% ± 1.6 for HUVEC cells and 16.2% ± 2.1 for SKOV3 cells), especially in VE-DDP-Pro (8.2% ± 2 for HUVEC cells and 7.3% ± 1.5 for SKOV3 cells) (Fig. S8D-E). On the basis of these results, the *anti*-EDV activity in HUVEC cells and *anti*-VM activity in SKOV3 cells were obeyed the

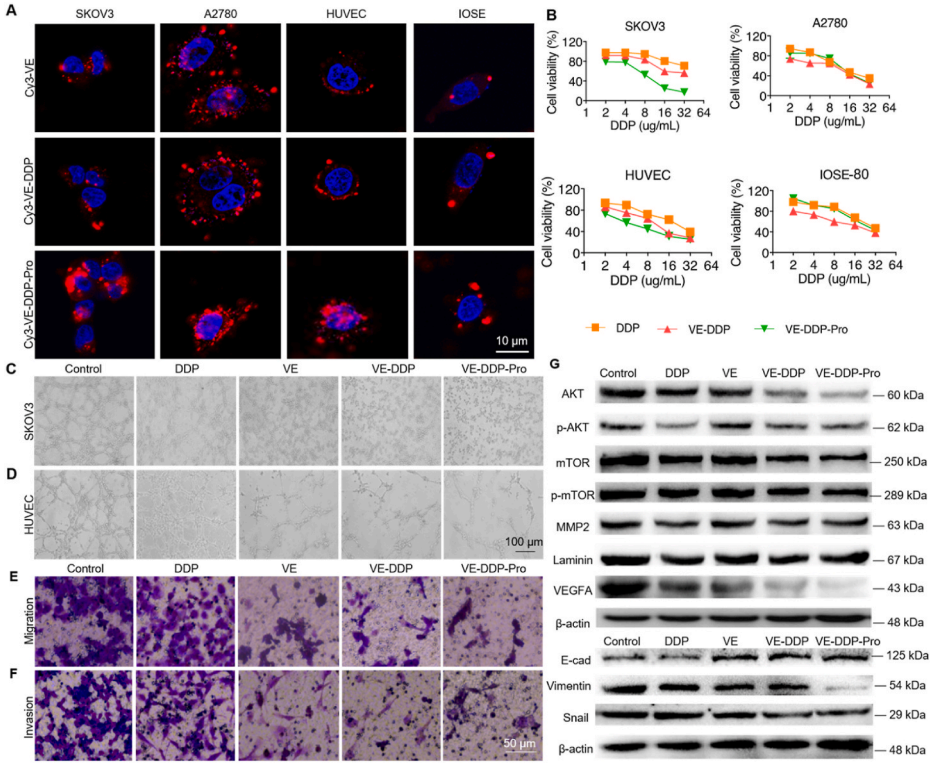

Fig. 2. The targeting ability, cytotoxicities, *anti*-EDV and *anti*-VM capacities of VE-DDP-Pro *in vitro*. (A) laser scanning confocal imaging of the cellular uptake ability of Cy3 labeled VE, VE-DDP and VE-DDP-Pro by SKOV3, A2780, HUVEC and IOSE-80-80 cells. Hoechst staining (blue) and Cy3-nanoparticles visualized using fluorescence (red). Scale bar: 10 μm. (B) Cytotoxicities of DDP, VE-DDP and VE-DDP-Pro were examined in SKOV3, A2780, HUVEC and IOSE-80-80 cells *via* MTT assay. Data are presented as means ± SD (n = 4). (C) The assessment of VM tubular structures in SKOV3 cells by 3D culture. (D) The assessment of EDV tubular structures in HUVEC. (E) Migration and (F) invasion experiments were conducted in SKOV3 cells treated with DDP, VE, VE-DDP and VE-DDP-Pro. Data are presented as means ± SD from five independent images (***$P < 0.001$). (G) The protein expression of AKT, p-AKT, mTOR, p-mTOR, MMP-2, Laminin, VEGFA, E-cad, Vimentin and Snail was detected by Western blot in SKOV3 cells treated with PBS, DDP, VE, VE-DDP and VE-DDP-Pro. (each at the equivalent dose of VE and DDP). The data are presented as the means ± SD (n = 3), *$P < 0.05$, **$P < 0.01$, ***$P < 0.001$.

following order: VE-DDP-Pro > VE-DDP > VE > DDP, suggesting the good *anti*-EDV and *anti*-VM capacity of our VE-DDP-Pro. Next, we tested the migration and invasion ability of DDP, VE, VE-DDP and VE-DDP-Pro in SKOV3 cells (Fig. 2E–F). It was obviously observed DDP (120.04% ± 6.74 for migration and 98.67% ± 11.88 for invasion) could not inhibit the migration and invasion of SKOV3 cells. Interestingly, VE (27.70% ± 5.57 for migration and 50.92% ± 9.16 for invasion), VE-DDP (33.02% ± 10.03 for migration and 57.11% ± 4.55 for invasion) and VE-DDP-Pro (31.21% ± 1.94 for migration and 60.12% ± 6.85 for invasion) could suppress cell migration and invasion for SKOV3 cells, especially VE presented similar the inhibitory ability of migration and invasion as VE-DDP and VE-DDP-Pro (Fig. S8F-G). These results suggested the involvement of VE in VE-DDP and VE-DDP-Pro played important role on restricting the migration and invasion ability of tumor cells.

3.5. Molecular mechanism of VE-DD-Pro in vitro

It was reported that the direct interaction between the integrin $\alpha_v\beta_3$ or $\alpha_5\beta_1$ and MMP-2 could promote angiogenesis and tumor growth. And transcriptional suppression of MMP-2 resulted in decreased VEGF expression in several tumor cells, which led to decreased angiogenesis. Thus, cRGD binding with integrin $\alpha_v\beta_3$ or $\alpha_5\beta_1$ could present promising *anti*-EDV capability by down-regulating MMP-2/VEGF expression [20]. Laminin was essential in the VM formation, while AKT-mTOR signal pathway could modulate MMP-2 expression important for cleavage of the Laminin. EMT is a dynamic biological process characterized by loss of epithelial feature and the acquisition of mesenchymal feature as well as a change in cellular morphology [39], and EMT regulated by AKT-mTOR signal pathway subsequently improves the motility of tumor cells [40]. It was found tumor cells involved in VM formation exhibit endothelial phenotypes of mesenchymal cells which is similar to process of EMT [41]. We previously found that cRGD binding with integrin $\alpha_v\beta_3$ could inhibit VM formation by regulating AKT/mTOR/MMP-2/Laminin but also reducing EMT [21]. Thus, we assayed the expression of MMP-2/VEGF, AKT/mTOR/MMP-2/Laminin and EMT-associated proteins (E-cad, Vimentin and Snail) in SKOV3 cells (Fig. 2G and S10). Compared with DDP, VE-DDP and VE-DDP-Pro could significantly down-regulate the expression of AKT, mTOR and their phosphorylation, VEGFA, MMP-2, Laminin, Vimentin and Snail, while the E-cad expression was up-regulated. Also, VE-DDP-Pro had stronger regulation ability than VE-DDP. Thus it was confirmed that VE-DDP-Pro could efficiently inhibit EDV and VM formation through regulating MMP-2/VEGF, AKT/mTOR/MMP-2/Laminin and AKT/mTOR/EMT signal pathways in ovarian cancer cells. Collectively, our VE-DDP-Pro possesses excellent cellular internalization, enhanced cytotoxicity, *anti*-EDV and *anti*-VM capacities *in vitro*, which would be beneficial to highly efficient treatment of the metastatic ovarian cancer.

3.6. Biodistribution and cancer-targeting capacity of VE-DDP-Pro in vivo

The biodistribution and cancer-targeting ability of VE-DDP-Pro were comprehensively investigated by using living imaging and ICP-MS methods. A successful orthotopic ovarian cancer model is a prerequisite for *in vivo* clinical evaluation. A nude mouse orthotopic ovarian cancer model was successfully constructed by directly injecting a bioluminescence SKOV3-Luc cell suspension into ovarian parenchyma of mouse and then by developing of primary tumor, ascites and distant organ metastasis (Fig. S11). The fluorescent dye Cy7-NH_2 was conjugated with heparin of VE, VE-DDP and VE-DDP-Pro and Cy7-VE, Cy7-VE-DDP and Cy7-VE-DDP-Pro were employed to real-time monitor their targeting abilities and biodistributions *via* tail vein injection. The biodistributions of Cy7-VE-DDP and Cy7-VE-DDP-Pro were monitored at 24 h, 48 h, 72 h (Fig. 3A), 96 h and 120 h (Fig. S12A-D), and mice were subsequently sacrificed to obtain organs and the whole ovary with primary tumor. We analyzed the Cy7 fluorescent intensity of organs and orthotopic tumors in ovary, which was merged with bioluminescence of SKOV3-Luc cells. As shown in Fig. 3A, Cy7-VE and Cy7-VE-DDP presented the similar cancer-targeting ability and biodistribution property, indicating the introduction of DDP could not change the biodistribution ability of Cy7-VE due to low DDP loading in VE-DDP. And Cy7-VE-DDP-Pro had more efficient capacities in retention times and cancer-targeting capacity in comparison with Cy7-VE and Cy7-VE-DDP, which is

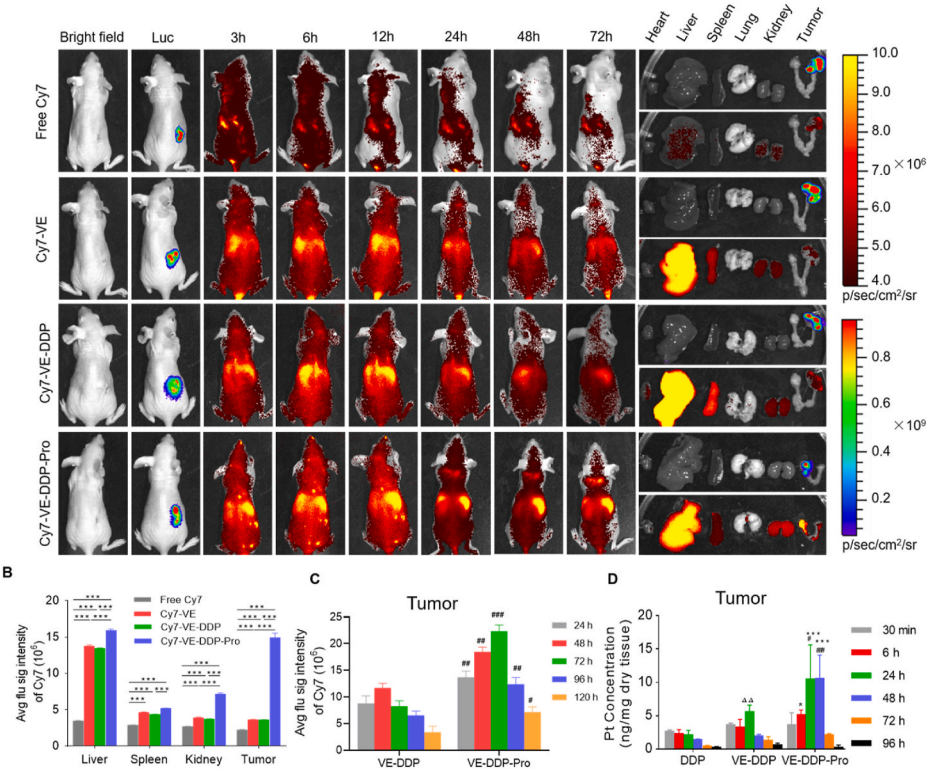

Fig. 3. *In vivo* biodistribution and tumor-targeting ability of nanoparticles. (A) Real-time imaging of *in vivo* biodistribution and tumor targeting. Mice were administered SKOV3-Luc cells into ovarian parenchyma *via* directly injection, and 4 days later, treated with a single dose of free Cy7, Cy7-VE, Cy7-VE-DDP and Cy7-CE-DDP-Pro (DDP 2 μg/g, three mice per group) *via* tail vein injection. Luminescence signals were examined at different time-points. After 72 h, mice were sacrificed and their organs and tumors obtained for direct monitoring of Luminescence. (B) Fluorescent intensity of their organs and primary tumors determined by real-time imaging. (C) *In vivo* tumor targeting capacity and variations of Cy7-VE-DDP and Cy7-VE-DDP-Pro over time in orthotopic tumor in ovary. Mice treated with Cy7-VE-DDP and Cy7-CE-DDP-Pro (DDP 2 μg/g, three per group) were sacrificed at 24, 48, 72, 96 and 120 h, and primary tumors in ovary obtained for analysis. (D) ICP-MS analysis of Pt concentration in orthotopic tumor of SKOV3 bearing nude mice treated with DDP, VE-DDP and VE-DDP-Pro at different time. Data are presented as means ± SD (n = 3), $^*P < 0.05$, $^{**}P < 0.01$, $^{***}P < 0.001$ (DDP vs VE-DDP-Pro), $\#P < 0.05$, $\#\#P < 0.01$, $\#\#\#P < 0.001$ (VE-DDP vs VE-DDP-Pro), $\Delta\Delta P < 0.01$ (DDP vs VE-DDP).

consistent with *in vitro* cellular uptake results. The highest fluorescence signals appeared in tumor, liver, kidney and spleen in orders, while nearly no fluorescence signal was detected in the heart and lung (Fig. 3B). The *in vivo* cancer targeting capacities and variations of Cy7-VE-DDP and Cy7-VE-DDP-Pro over time are presented in Fig. 3C and Fig. S12E. The results showed that the highest fluorescence signal of Cy7-VE-DDP appeared at 48 h and declined afterwards, while the highest signal of Cy7-VE-DDP-Pro was delayed to 72 h and the signal at 120 h was still as strong as that of Cy7-VE-DDP at 72 h, indicating protamine could delay VE carrier release.

In order to accurately characterize DDP biodistribution, we used ICP-MS to detect Pt concentration in rat serum at different time points after intravenous injection of DDP, VE-DDP and VE-DDP-Pro (Fig. S13A). At initial 30 min, VE-DDP-Pro group exhibit maximal Pt concentration in blood (0.852 ± 0.112 ng/mg), while VE-DDP group and DDP group were 0.570 ± 0.570 ng/mg and 0.421 ± 0.076 ng/mg, respectively. It was observed Pt concentration of DDP in blood presented dramatically reduced tendency and there was low Pt concentration (0.041 ± 0.023 ng/mg) at 12 h. In comparison, VE-DDP group and VE-DDP-Pro group still remained fairly high concentration of Pt (0.298 ± 0.085 ng/mg and 0.441 ± 0.105 ng/mg). However, Pt concentration of VE-DDP group was obviously decreased at 24 h while VE-DDP-Pro remained slow released effect. Collectively, VE-DDP and VE-DDP-Pro had significantly extended circulation time, and VE-DDP-Pro presented best pharmacokinetics property, indicating the introduction of protamine enhanced VE-DDP stability *in vivo*. In addition, we detected Pt concentration of DDP, VE-DDP and VE-DDP-Pro groups in liver, spleen, kidney and tumor of mouse at different time (Fig. 3D and S13B). It showed Pt concentration of VE-DDP and VE-DDP-Pro in tumor was higher than that of DDP due to cancer targeting effect of VE, and Pt concentration of VE-DDP-Pro was higher compared with that of VE-DDP due to cytomembrane penetration effect of protamine. In addition, Pt concentration in DDP group (2.76 ± 0.13 ng/mg dry tissue) obtained highest at initial time while the highest Pt concentration (5.71 ± 0.88 ng/mg dry tissue) was obtained at 24 h for VE-DDP and for VE-DDP-Pro 24 h and 48 h could maintain the highest concentration of Pt (10.59 ± 5.03 ng/mg dry tissue 24 h, 10.66 ± 3.44 ng/mg dry tissue 48 h), which was inconsistent with the results of living imaging. It possibly attributed to different metabolism rate between carrier and drug. The results suggested the cytomembrane penetration effect of protamine could further enhance VE-DDP accumulation at tumor and further delay release of DDP in tumor. Compared with DDP, VE-DDP and VE-DDP-Pro showed higher cumulative accumulation in liver, spleen, kidney, indicating VE-DDP and VE-DDP-Pro prolonged blood circulation (Fig. S13). According to the results of biodistribution, our self-assembled VE-DDP-Pro could specifically deliver DDP to ovarian cancer and significantly increase drug accumulation in tumor, facilitating VE-DDP-Pro to enhance the therapeutic effect to tumor cells and reduce the toxic side effects to normal cells [29,34]. Thus, the excellent targeting effect of VE-DDP-Pro for ovarian cancer suggested its anti-tumor activities *in vivo* were worth to be expected.

3.7. Anti-proliferation and -metastasis activity of VE-DDP-Pro in vivo

Next, we investigated the inhibitory capacity of our VE-DDP-Pro in the development and metastasis of ovarian cancer. Mice with orthotopic ovarian cancer were randomly divided into four groups (each with five mice, with equal average bioluminescence signals). Mice treated with PBS were used as the control group. The development of ovarian cancer was traced by capturing bioluminescence signals of SKOV3-Luc cells. DDP, VE-DDP and VE-DDP-Pro (at an equivalent dose of 2 μg/g DDP) were administered *via* intravenous injection at three-day intervals, respectively. After that, the bioluminescence of SKOV3-Luc cells was measured every four days. As shown in Fig. 4A, ovarian cancer in the control group developed rapidly and began to metastasize on day 4 after the first treatment, which was systemically metastasized by day 20. In the DDP treatment group, ovarian cancer was effectively suppressed at an early stage (day 8). However, at the later stages, tumor was gradually developed until systemic metastasis by day 20, indicating that rapidly proliferating ovarian cancer cells led to metastasize and ultimately resisted to DDP. In contrast, the development and metastasis of ovarian cancer treated with VE-DDP-Pro was effectively suppressed throughout the treatment period. And, tumor proliferation was significantly inhibited, through which no metastasis was observed in mice treated with VE-DDP-Pro by real-time imaging. The proliferation rate of SKOV3-Luc cells in the VE-DDP-Pro group was 6.52 ± 2.99 at day 20, which was significantly lower than that of control (631.67 ± 207.08) and DDP (390.27 ± 249.74) groups (Fig. 4B). It was found mice receiving the free DDP demonstrated a sharp decrease in the body weight of mice. Body

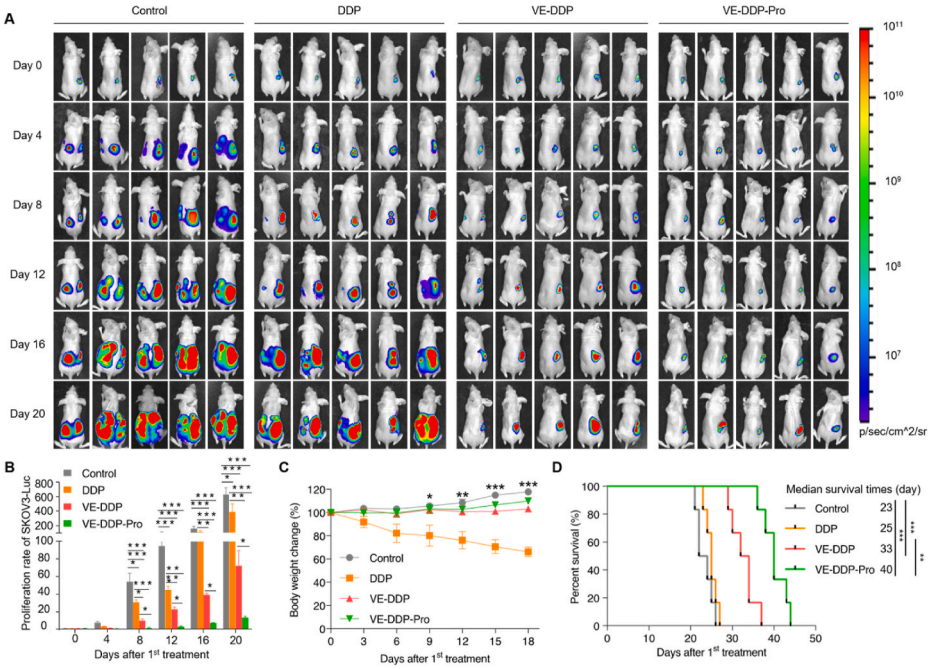

Fig. 4. VE-DDP and VE-DDP-Pro inhibit ovarian cancer metastasis *in vivo*. (A) Mice were administered SKOV3-Luc cells into ovarian parenchyma *via* directly injection, followed by treatment and measurement of bioluminescence after 3 days (day 0). Mice of the control group were treated with PBS and those in the other three groups with DDP, VE-DDP and VE-DDP-Pro (DDP 2 μg/g, five mice per group) at 3-day intervals. Bioluminescence was measured every 4 days. (B) Proliferation rate of SKOV3-Luc cells calculated using the following equation: proliferation rate = luminescence signal intensity of day n/average luminescence signal intensity of day 0. Data are presented as means ± SD (n = 5), $*P < 0.05$, $***P < 0.001$. (C) Body weight change of the mouse during the treatment period. Blue arrowheads indicate the injection time. (D) Survival curve and median survival times of mouse treated with PBS, DDP, VE-DDP and VE-DDP-Pro. Data are presented as the means ± SD (n = 6), $**P < 0.01$, $***P < 0.001$.

weight loss of 38.1 ± 3.50% on 18th day after treatment with a dose of 2 μg/g DDP. In contrast, mice treated with VE-DDP and VE-DDP-Pro did not show any significant weight loss, just similar to that of control groups (Fig. 4C), suggesting the severe toxicity of free DDP against mice. H&E staining showed obvious focal necrosis and inflammation were detectable in livers of mouse treated with DDP while no symptoms were evident in other groups. In addition, it was observed most proximal tubular epithelial cells became edematous or exfoliated from the basement membrane causing broadened renal tubules, and numerous macrophages were present in spleens. It indicated DDP induced hepatotoxicity, renal toxicity and injured spleen thereby resulting in decreased body weight (Fig. S14 and S15). The excellent properties of VE-DDP-Pro *in vitro* and *in vivo*, including targeting effect to tumor cells, pH-sensitivity in tumor tissues, pharmacokinetics property, were beneficial them to enhance the therapeutic effect to tumor and minimize the toxic side effects. We then evaluated the overall survival of all the treatment groups for the SKOV3-Luc orthotopic ovarian cancer model (Fig. 4D). It was observed that mice treated with VE-DDP-Pro presented the highest median survival in comparison with other groups. The order of median survival was as follows: VE-DDP-Pro (40 days) > VE-DDP (33 days) > DDP (25 days) > control (23 days).

To further assess the anti-tumor activity of our system, mice were sacrificed on day 20 to obtain primary tumors, multi-organ metastatic nodules (including those in the peritoneal cavity, and mesentery metastatic nodules). As shown in Fig. 5A–C, the average primary tumor volume and weight treated by VE-DDP-Pro (volume, 12.99 ± 9.71 mm^3; weight, 84.60 ± 46.73 mg) were significantly lower than those of control (volume, 108.83 ± 25.08 mm^3; weight, 591.20 ± 115.01 mg), DDP (volume, 79.56 ± 28.39 mm^3; weight, 398.76 ± 133.59 mg) and VE-DDP (volume, 25.02 ± 12.84 mm^3; weight, 218.18 ± 132.88 mg). In addition, mice treated with PBS and DDP were found the metastatic nodules in peritoneal cavity (Fig. S16A). We found obviously increased abdominal circumferences of mice treated with PBS and DDP compared with that of VE-DDP and VE-DDP-Pro group (Fig. 5D). After dissection, slight malignant ascites could be detected in the control group and DDP group determined by the chest ascites smear, but was absent in the VE-DDP group and VE-DDP-Pro group (Fig. 5E). It showed a lot of blood cells and white blood cells in the chest ascites smears, indicating mice treated with PBS and DDP induced the formation of malignant ascites (Fig. S17). We subsequently examined mesentery metastasis by detecting bioluminescence and directly counting nodule numbers (Fig. 5F, G and S16B). Compared to the control group and DDP group, there is almost no metastasis was observed in mice treated with VE-DDP-Pro. In VE-DDP treatment group, there is a few metastatic nodules (4.40 ± 4.16) along with extremely low luminescence signals (11.06 ± 11.38 × 10^8). However, several nodules and high luminescence signals were detected in mice treated with PBS (30.40 ± 3.21, 300.50 ± 41.74 × 10^8) and DDP (23.20 ± 3.49, 210.32 ± 50.32 × 10^8). Metastatic nodules on mesentery were further analyzed *via* H&E staining and the results confirmed there was no mesentery metastasis in VE-DDP-Pro group and mesentery metastasis in control and DDP groups (Fig. 5H–I), and the pancreas was invaded by cancer cells and normal structure destroyed (Fig. S18). Collectively, our VE-DDP-Pro had a significant capacity to efficiently suppress the development and metastasis of orthotopic ovarian cancer and reduce side toxicity *via* specific delivery and enhancing tumor accumulation.

3.8. Mechanism of anti-proliferation and -metastasis activity for VE-DDP-Pro in vivo

To better understand the mechanisms of our VE-DDP-Pro to inhibit tumor proliferation and metastasis associated with EDV and VM, we further investigated the expression of MMP-2/VEGF and AKT-mTOR signal pathway in SKOV3 xenograft tissue sections from mice treated with PBS, DDP, VE-DDP and VE-DDP-Pro (Fig. 5J). It showed VE-DDP and VE-DDP-Pro could down-regulate the expression of VEGFA, MMP-2, AKT and mTOR phosphorylation, Laminin, Vimentin and Snail, while could up-regulate E-cad expression (Fig. S19). The results suggested that our VE-DDP-Pro can significantly inhibit the formation of EDV and VM by regulating signaling pathway of MMP-2/VEGF expression, AKT/mTOR/MMP-2/Laminin and AKT/mTOR/EMT, allowing the effectively suppressing the development and metastasis of ovarian cancer. In addition, the immunohistochemical analysis of primary tumors from control, DDP, VE-DDP and VE-DDP-Pro groups and metastatic tumor come from control or DDP groups were further conducted. Firstly, the cell proliferation marker, Ki-67, was employed to evaluate anti-

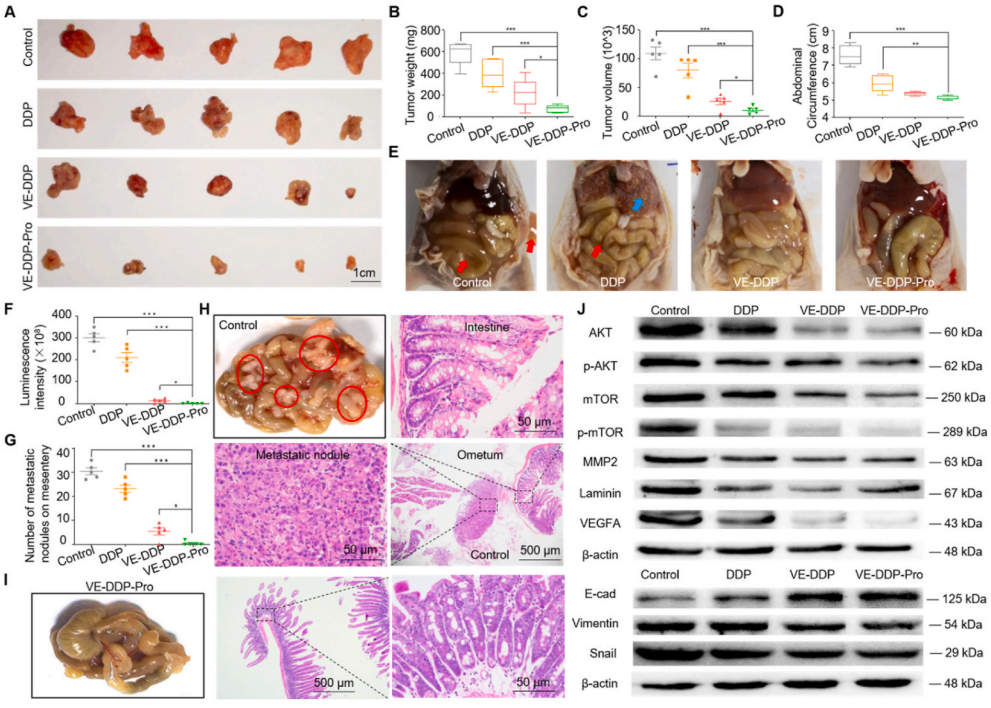

Fig. 5. VE-DDP and VE-DDP-Pro inhibit ovarian cancer metastasis *in vivo*. (A) Excised ovarian primary tumors from each treatment group. (B) Tumor weights of each treatment group. (C) Tumor volumes from each treatment group. (D) The measurement of abdominal circumference of mice treated by each group. (E) Malignant ascites and abdominal circumference of mice. Red arrowhead indicates malignant ascites and blue arrowhead indicates injured liver. (F) Luminescence of metastatic nodules on mesentery were analyzed. (G) Number of metastatic nodules on mesentery were analyzed. (H) Magnified image of mesentery treated with control group and H&E staining images of mesentery metastasis of the control group. Red circles indicate metastatic nodules on the mesentery. (I) Magnified image of mesentery treated with VE-DDP-Pro and H&E staining images of mesentery treated with VE-DDP-Pro. Data are presented as means ± SD (n = 5), $^*P < 0.05$, $^{**}P < 0.01$, $^{***}P < 0.001$. (J) The protein expression of AKT, p-AKT, mTOR, p-mTOR, MMP-2, Laminin, VEGFA, E-cad, Vimentin and Snail was detected by Western blot in tumor tissues of PBS, DDP, VE-DDP and VE-DDP-Pro groups.

proliferative ability of VE-DDP-Pro [42]. The result demonstrated that the tumor Ki-67 indices of control, metastasis and DDP groups were much higher than that of VE-DDP-Pro groups (Fig. 6A and G), suggesting that our VE-DDP-Pro possessed good anti-proliferation effects. In addition, DDP primarily induces cell death by apoptosis which can be initiated by DNA damage [43]. In this study, the cleaved caspase-3 expression was selected to investigate the apoptosis ability of VE-based drug delivery system. The result demonstrated that the cleaved caspase-3 expression of VE-DDP-Pro was higher than that of control, metastatic tumor, DDP and VE-DDP groups, suggesting that the introduction of VE and protamine into the VE-DDP-Pro could significantly enhance the efficacy of DDP-mediated ovarian cancer cell apoptosis (Fig. 6B and H). Next, CD34 and CD34/Periodic Acid Schiff (PAS) double staining were conducted to examine anti-angiogenesis ability [44–46]. In general, $CD34^+$ expression suggested the formation of EDV in ovarian cancer cells, while $CD34^-/PAS^+$ vascular-like structures indicated the formation of VM [45,46]. As shown in Fig. 6C and D, a large number of EDV structures ($CD34^+$ expression) and VM structures ($CD34^-/PAS^+$ expression) were formed in the control group, metastasis and DDP group, while they were nearly not observed in the VE-DDP-Pro groups (Fig. 6I and J). And SKOV3 cells were detected in $CD34^+$ structures in the control group, metastasis and DDP group (Fig. S20). These results indicated the hematogenous metastasis based on EDV and VM is an essential pathway of metastasis in ovarian cancer, and our VE-DDP-Pro can effectively suppress the formation of EDV and VM. We next investigated the influence of MMP-2 and VEGF on angiogenesis in VE-DDP and VE-DDP-Pro groups. As expected, high expression of MMP-2 and VEGF in primary tumors and metastatic tumor of control and DDP groups were observed. Especially, in DDP group, VEGF was found highly expressed in tumor tissues around the neovascularization area (Fig. S21). While, VE-DDP-Pro groups exhibited low expression of MMP-2 and VEGF (Fig. 6E, F, K and L). Also, tumors from control group and DDP group, and metastatic tumors from control or DDP groups represented similar pathological characteristic. These results demonstrated that our VE-DDP-Pro can significantly inhibit the formation of EDV and VM thereby facilitating to effectively suppress the development and metastasis of ovarian cancer. Notably, anti-angiogenic therapy generally served as an adjuvant modality of chemotherapy to inhibit cancer development and metastasis. Due to fast proliferation ability of cancer cells in orthotopic ovary tissue, single anti-angiogenic therapy could not effectively inhibit cancer development and metastasis and thus we did not conduct the compared *in vivo* experiments of VE to further verify its *anti*-EDV and –VM effect *in vivo*. Thus, multi-modality therapy combined with chemotherapy could be effective treatment for inhibit cancer growth and improve tolerance [47–49].

4. Conclusions

In summary, we have fabricated a self-assembled VE-DDP-Pro nanoparticle that integrating DDP triggered anti-proliferation, Pro induced the cellular uptake improvement, and VE nanoparticles regulated self-*anti*-EDV and -VM ability. Thus, VE-DDP-Pro exhibit excellent cancer-targeting, cellular internalization ability, and significant enhancement of the treatment efficacy for malignant metastasis ovarian cancer. We strongly believe that the integration of anti-proliferation and anti-angiogenesis properties based on EDV and VM would thus present an effective strategy to improve the efficacy of chemotherapeutic drugs for metastatic tumor and represents a promising prospect for clinical applications.

Declaration of interests

The authors declare that they have no known competing financial interests or personal relationships that could have appeared to influence the work reported in this paper.

CRediT authorship contribution statement

Jiamao Luo: Conceptualization, Investigation, Methodology, Validation, Writing – original draft. **Xinxian Zhong:** Investigation, Methodology, Validation. **Yingming Peng:** Investigation, Methodology, Validation. **Chenyuan Hao:** Resources. **Xiaomei Liang:** Investigation, Methodology, Validation, Formal analysis. **Yulu Yang:** Methodology, Validation. **Xiubo Shi:** Data curation. **Xuncai Chen:** Resources. **Xiao Yi:** Data curation. **Xiaoxuan Li:** Formal analysis. **Jianhua Wu:** Investigation, Methodology. **Jinheng Li:** Data curation. **Qian Xiao:**

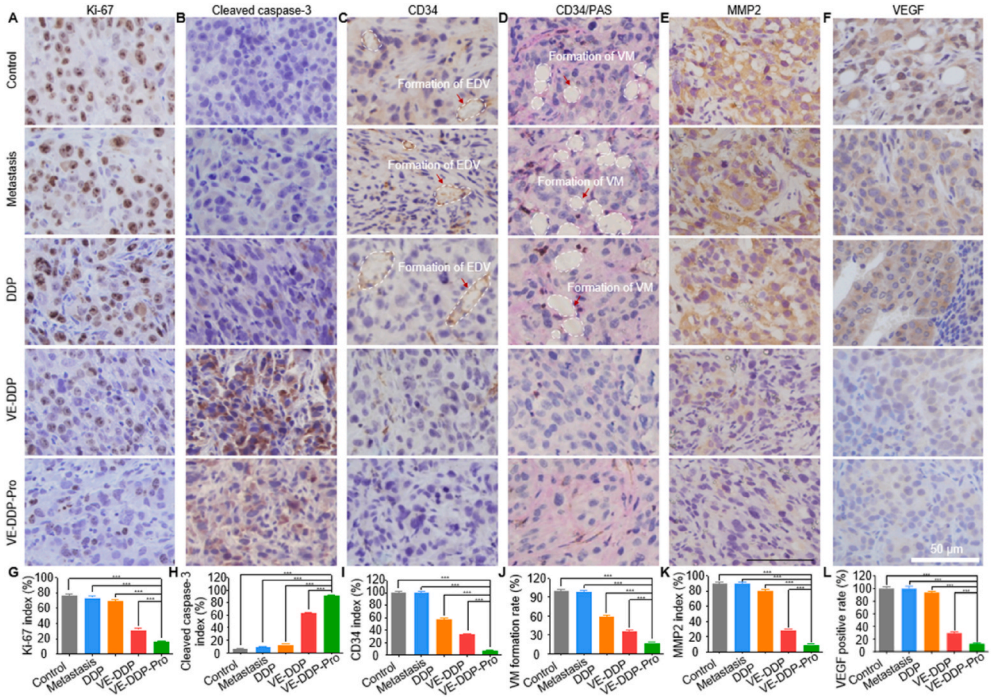

Fig. 6. Immunohistochemical analysis of tumor from different treatment groups and metastatic tumor from control or DDP. The tumor was stained by (A and G) Ki-67; (B and H) cleaved caspase-3; (C and I) CD34, Red arrowheads indicate $CD34^+$ structures defined as EDV; (D and J) CD34/PAS double staining, Red arrowheads indicate $CD34^-/PAS^+$ vascular-like structures defined as VM; (E and K) MMP-2; (F and L) VEGF. All statistical data are presented as means ± SD (n = 5), $^{***}P < 0.001$.

Investigation. **Chentian Wu:** Investigation. **Ruojing Lu:** Methodology. **Yao Pan:** Methodology. **Xuejiao Wang:** Formal analysis. **Jun-Bing Fan:** Validation, Conceptualization, Funding acquisition, Supervision, Writing – review & editing. **Yifeng Wang:** Conceptualization, Funding acquisition, Supervision. **Ying Wang:** Validation, Conceptualization, Funding acquisition, Supervision, Writing – review & editing.

Acknowledgments

We thank Hongfen Shen for help with flow cytometry assay. This work was supported by grants from the National Natural Science Foundation of China (No. 22075127, 81773291, 21872158), Frontier Research Program of Guangzhou Regenerative Medicine and Health Guangdong Laboratory (2018GZR110105005) and Natural Science Foundation of Guangdong Province (2021A1515011638).

Appendix A. Supplementary data

Supplementary data to this article can be found online at https://doi.org/10.1016/j.bioactmat.2021.10.037.

References

[1] R.L. Siegel, K.D. Miller, A. Jemal, Cancer statistics, 2020, CA, A Cancer J Clin 70 (1) (2020) 7–30.
[2] D. Holmes, Ovarian cancer: beyond resistance, Nature 527 (7579) (2015). S217-S217.
[3] A.J. Maniotis, R. Folberg, A. Hess, E.A. Seftor, L.M. Gardner, J. Pe'er, J.M. Trent, P. S. Meltzer, M.J. Hendrix, Vascular channel formation by human melanoma cells in vivo and in vitro: vasculogenic mimicry, Am. J. Pathol. 155 (3) (1999) 739–752.
[4] R.E.B. Seftor, A.R. Hess, E.A. Seftor, D.A. Kirschmann, K.M. Hardy, N. V. Margaryan, M.J.C. Hendrix, Tumor cell vasculogenic mimicry: from controversy to therapeutic promise, Am. J. Pathol. 181 (4) (2012) 1115–1125.
[5] A.K. Sood, M.S. Fletcher, C.M. Zahn, L.M. Gruman, J.E. Coffin, E.A. Seftor, M.J. C. Hendrix, The clinical significance of tumor cell-lined vasculature in ovarian carcinoma: implications for anti-vasculogenic therapy, Cancer Biol. Ther. 1 (6) (2002) 661–664.
[6] E. Wagenblast, M. Soto, S. Gutiérrez-Ángel, C.A. Hartl, A.L. Gable, A.R. Maceli, N. Erard, A.M. Williams, S.Y. Kim, S. Dickopf, J.C. Harrell, A.D. Smith, C.M. Perou, J.E. Wilkinson, G.J. Hannon, S.R.V. Knott, A model of breast cancer heterogeneity reveals vascular mimicry as a driver of metastasis, Nature 520 (7547) (2015) 358–362.
[7] F. Zhang, H. Lin, K. Cao, H. Wang, J. Pan, J. Zhuang, X. Chen, B. Huang, D. Wang, S. Qiu, Vasculogenic mimicry plays an important role in adrenocortical carcinoma, Int. J. Urol. 23 (5) (2016) 371–377.
[8] B. Sun, S. Zhang, X. Zhao, W. Zhang, X. Hao, Vasculogenic mimicry is associated with poor survival in patients with mesothelial sarcomas and alveolar rhabdomyosarcomas, Int. J. Oncol. 25 (6) (2004) 1609–1614.
[9] L. Moserle, G. Jiménez-Valerio, O. Casanovas, Antiangiogenic therapies: going beyond their limits, Cancer Discov. 4 (1) (2014) 31–41.
[10] A. de Gramont, E. Van Cutsem, H.-J. Schmoll, J. Tabernero, S. Clarke, M.J. Moore, D. Cunningham, T.H. Cartwright, J.R. Hecht, F. Rivera, S.-A. Im, G. Bodoky, R. Salazar, F. Maindrault-Goebel, E. Shacham-Shmueli, E. Bajetta, M. Makrutzki, A. Shang, T. André, P.M. Hoff, Bevacizumab plus oxaliplatin-based chemotherapy as adjuvant treatment for colon cancer (AVANT): a phase 3 randomised controlled trial, Lancet Oncol. 13 (12) (2012) 1225–1233.
[11] C. Aghajanian, S.V. Blank, B.A. Goff, P.L. Judson, M.G. Teneriello, A. Husain, M. A. Sovak, J. Yi, L.R. Nycum, OCEANS: a randomized, double-blind, placebo-controlled phase III trial of chemotherapy with or without bevacizumab in patients with platinum-sensitive recurrent epithelial ovarian, primary peritoneal, or fallopian tube cancer, J. Clin. Oncol. 30 (17) (2012) 2039–2045.
[12] B.J. Giantonio, P.J. Catalano, N.J. Meropol, P.J. O'Dwyer, E.P. Mitchell, S. R. Alberts, M.A. Schwartz, A.B. Benson, E. Eastern Cooperative Oncology Group Study, Bevacizumab in combination with oxaliplatin, fluorouracil, and leucovorin (FOLFOX4) for previously treated metastatic colorectal cancer: results from the Eastern Cooperative Oncology Group Study E3200, J. Clin. Oncol. 25 (12) (2007) 1539–1544.
[13] E. Pujade-Lauraine, F. Hilpert, B. Weber, A. Reuss, A. Poveda, G. Kristensen, R. Sorio, I. Vergote, P. Witteveen, A. Bamias, D. Pereira, P. Wimberger, A. Oaknin, M.R. Mirza, P. Follana, D. Bollag, I. Ray-Coquard, Bevacizumab combined with chemotherapy for platinum-resistant recurrent ovarian cancer: the AURELIA open-label randomized phase III trial, J. Clin. Oncol. 32 (13) (2014) 1302–1308.
[14] G. Zalcman, J. Mazieres, J. Margery, L. Greillier, C. Audigier-Valette, D. Moro-Sibilot, O. Molinier, R. Corre, I. Monnet, V. Gounant, F. Rivière, H. Janicot, R. Gervais, C. Locher, B. Milleron, Q. Tran, M.-P. Lebitasy, F. Morin, C. Creveuil, J.-J. Parienti, A. Scherpereel, I. French, Cooperative Thoracic, Bevacizumab for newly diagnosed pleural mesothelioma in the Mesothelioma Avastin Cisplatin Pemetrexed Study (MAPS): a randomised, controlled, open-label, phase 3 trial, Lancet 387 (10026) (2016) 1405–1414.
[15] P.G. Corrie, A. Marshall, J.A. Dunn, M.R. Middleton, P.D. Nathan, M. Gore, N. Davidson, S. Nicholson, C.G. Kelly, M. Marples, S.J. Danson, E. Marshall, S. J. Houston, R.E. Board, A.M. Waterston, J.P. Nobes, M. Harries, S. Kumar, G. Young, P. Lorigan, Adjuvant bevacizumab in patients with melanoma at high risk of recurrence (AVAST-M): preplanned interim results from a multicentre, open-label, randomised controlled phase 3 study, Lancet Oncol. 15 (6) (2014) 620–630.
[16] O. Casanovas, D.J. Hicklin, G. Bergers, D. Hanahan, Drug resistance by evasion of antiangiogenic targeting of VEGF signaling in late-stage pancreatic islet tumors, Cancer Cell 8 (4) (2005) 299–309.
[17] G.C. Jayson, R. Kerbel, L.M. Ellis, A.L. Harris, Antiangiogenic therapy in oncology: current status and future directions, Lancet 388 (10043) (2016) 518–529.
[18] T. Xiang, Y.-X. Lin, W. Ma, H.-J. Zhang, K.-M. Chen, G.-P. He, X. Zhang, M. Xu, Q.-S. Feng, M.-Y. Chen, M.-S. Zeng, Y.-X. Zeng, L. Feng, Vasculogenic mimicry formation in EBV-associated epithelial malignancies, Nat. Commun. 9 (1) (2018) 5009.
[19] D. Sun, S. Zhou, W. Gao, What went wrong with anticancer nanomedicine design and how to make it right, ACS Nano 14 (10) (2020) 12281–12290.
[20] B. Felding-Habermann, Integrin adhesion receptors in tumor metastasis, Clin. Exp. Metastasis 20 (3) (2003) 203–213.
[21] J. Tang, J. Wang, L. Fan, X. Li, N. Liu, W. Luo, J. Wang, Y. Wang, Y. Wang, cRGD inhibits vasculogenic mimicry formation by down-regulating uPA expression and reducing EMT in ovarian cancer, Oncotarget 7 (17) (2016) 24050–24062.
[22] Y. Wang, L. Tong, J. Wang, J. Luo, J. Tang, L. Zhong, Q. Xiao, W. Niu, J. Li, J. Zhu, H. Chen, X. Li, Y. Wang, cRGD-functionalized nanoparticles for combination therapy of anti-endothelium dependent vessels and anti-vasculogenic mimicry to inhibit the proliferation of ovarian cancer, Acta Biomater. 94 (2019) 495–504.
[23] C. Müller, R. Schibli, Prospects in folate receptor-targeted radionuclide therapy, Front Oncol 3 (2013) 249.
[24] N. Amreddy, A. Babu, J. Panneerselvam, A. Srivastava, R. Muralidharan, A. Chen, Y.D. Zhao, A. Munshi, R. Ramesh, Chemo-biologic combinatorial drug delivery using folate receptor-targeted dendrimer nanoparticles for lung cancer treatment, Nanomedicine 14 (2) (2018) 373–384.
[25] F. Danhier, A. Le Breton, V. Préat, RGD-based strategies to target alpha(v) beta(3) integrin in cancer therapy and diagnosis, Mol. Pharm. 9 (11) (2012) 2961–2973.
[26] C.J. Avraamides, B. Garmy-Susini, J.A. Varner, Integrins in angiogenesis and lymphangiogenesis, Nat. Rev. Cancer 8 (8) (2008) 604–617.
[27] P.C. Brooks, R.A. Clark, D.A. Cheresh, Requirement of vascular integrin alpha v beta 3 for angiogenesis, Science 264 (5158) (1994) 569–571.
[28] F. Alam, T.A. Al-Hilal, S.W. Chung, J. Park, F. Mahmud, D. Seo, H.S. Kim, D.S. Lee, Y. Byun, Functionalized heparin-protamine based self-assembled nanocomplex for efficient anti-angiogenic therapy, J. Contr. Release 197 (2015) 180–189.
[29] M.-Q. Gong, J.-L. Wu, B. Chen, R.-X. Zhuo, S.-X. Cheng, Self-assembled polymer/inorganic hybrid nanovesicles for multiple drug delivery to overcome drug resistance in cancer chemotherapy, Langmuir 31 (18) (2015) 5115–5122.
[30] M. Yokoyama, T. Okano, Y. Sakurai, S. Suwa, K. Kataoka, Introduction of cisplatin into polymeric micelle, J. Contr. Release 39 (2) (1996) 351–356.
[31] N. Nishiyama, M. Yokoyama, T. Aoyagi, T. Okano, Y. Sakurai, K. Kataoka, Preparation and characterization of self-assembled polymer–metal complex micelle from cisdichlorodiammineplatinum(II) and poly(ethylene glycol)–poly (α,β-aspartic acid) block copolymer in an aqueous medium, Langmuir 15 (2) (1999) 377–383.
[32] H. Khurshid, S.H. Kim, M.J. Bonder, L. Colak, B. Ali, S.I. Shah, K.L. Kiick, G. C. Hadjipanayis, Development of heparin-coated magnetic nanoparticles for targeted drug delivery applications, J. Appl. Phys. 105 (7) (2009), 07B308.
[33] Q. Huang, J. Zhang, Y. Zhang, P. Timashev, X. Ma, X.J. Liang, Adaptive changes induced by noble-metal nanostructures in vitro and in vivo, Theranostics 10 (13) (2020) 5649–5670.
[34] J. Liu, Y. Huang, A. Kumar, A. Tan, S. Jin, A. Mozhi, X.J. Liang, pH-sensitive nano-systems for drug delivery in cancer therapy, Biotechnol. Adv. 32 (4) (2014) 693–710.
[35] R. Barbucci, A. Magnani, C. Roncolini, Thermodynamic and FT-IR spectroscopic studies on heparin-polycation interaction, Clin. Mater. 8 (1) (1991) 17–23.
[36] J. Wang, D.L. Rabenstein, Interaction of heparin and heparin-derived oligosaccharides with synthetic peptide analogues of the heparin-binding domain of heparin/heparan sulfate-interacting protein, Biochim. Biophys. Acta 1790 (12) (2009) 1689–1697.
[37] P. Moreno-Layseca, J. Icha, H. Hamidi, J. Ivaska, Integrin trafficking in cells and tissues, Nat. Cell Biol. 21 (2) (2019) 122–132.
[38] T. Tarui, N. Andronicos, R.P. Czekay, A.P. Mazar, K. Bdeir, G.C. Parry, A. Kuo, D. J. Loskutoff, D.B. Cines, Y. Takada, Critical role of integrin alpha 5 beta 1 in urokinase (uPA)/urokinase receptor (uPAR, CD87) signaling, J. Biol. Chem. 278 (32) (2003) 29863–29872.
[39] L.M. Cai, X.M. Lyu, W.R. Luo, X.F. Cui, Y.F. Ye, C.C. Yuan, Q.X. Peng, D.H. Wu, T. F. Liu, E. Wang, F.M. Marincola, K.T. Yao, W.Y. Fang, H.B. Cai, X. Li, EBV-miR-BART7-3p promotes the EMT and metastasis of nasopharyngeal carcinoma cells by suppressing the tumor suppressor PTEN, Oncogene 34 (17) (2015) 2156–2166.
[40] L. Liu, N. Wu, Y. Wang, X. Zhang, B. Xia, J. Tang, J. Cai, Z. Zhao, Q. Liao, J. Wang, TRPM7 promotes the epithelial-mesenchymal transition in ovarian cancer through the calcium-related PI3K/AKT oncogenic signaling, J. Exp. Clin. Cancer Res. 38 (1) (2019) 106.
[41] Z. Yang, B. Sun, Y. Li, X. Zhao, X. Zhao, Q. Gu, J. An, X. Dong, F. Liu, Y. Wang, ZEB2 promotes vasculogenic mimicry by TGF-β1 induced epithelial-to-mesenchymal transition in hepatocellular carcinoma, Exp. Mol. Pathol. 98 (3) (2015) 352–359.

[42] X. Sun, P.D. Kaufman, Ki-67: more than a proliferation marker, Chromosoma 127 (2) (2018) 175–186.
[43] C. Chen, C. Gao, Z. Yuan, Y. Jiang, Design, synthesis and biological evaluation of a novel platinum(II) complex possessing bioreductive groups for cancer therapy, Chin. Chem. Lett. 30 (1) (2019) 243–246.
[44] A. van Beurden, R.F. Schmitz, C.M. van Dijk, C.I. Baeten, Periodic acid Schiff loops and blood lakes associated with metastasis in cutaneous melanoma, Melanoma Res. 22 (6) (2012) 424–429.
[45] Y. Gao, H. Yu, Y. Liu, X. Liu, J. Zheng, J. Ma, W. Gong, J. Chen, L. Zhao, Y. Tian, Y. Xue, Long non-coding RNA HOXA-AS2 regulates malignant glioma behaviors and vasculogenic mimicry Formation via the MiR-373/EGFR axis, Cell. Physiol. Biochem. 45 (1) (2018) 131–147.
[46] B. Li, X. Mao, H. Wang, G. Su, C. Mo, K. Cao, S. Qiu, Vasculogenic mimicry in bladder cancer and its association with the aberrant expression of ZEB1, Oncol Lett 15 (4) (2018) 5193–5200.
[47] M. Zhou, Y. Xing, X. Li, X. Du, T. Xu, X. Zhang, Cancer cell membrane camouflaged Semi-Yolk@Spiky-Shell nanomotor for enhanced cell adhesion and synergistic therapy, Small 16 (39) (2020), e2003834.
[48] C. Liu, Y. Cao, Y. Cheng, D. Wang, T. Xu, L. Su, X. Zhang, H. Dong, An open source and reduce expenditure ROS generation strategy for chemodynamic/photodynamic synergistic therapy, Nat. Commun. 11 (1) (2020) 1735.
[49] C. Liu, D. Wang, S. Zhang, Y. Cheng, F. Yang, Y. Xing, T. Xu, H. Dong, X. Zhang, Biodegradable biomimic copper/manganese silicate nanospheres for chemodynamic/photodynamic synergistic therapy with simultaneous glutathione depletion and hypoxia relief, ACS Nano 13 (4) (2019) 4267–4277.